

Available online at www.sciencedirect.com

SciVerse ScienceDirect

<http://www.elsevier.com/locate/biombioe>

Supercapacitors using binderless composite monolith electrodes from carbon nanotubes and pre-carbonized biomass residues

N.H. Basri^a, M. Deraman^{a,*}, S. Kanwal^b, I.A. Talib^a, J.G. Manjunatha^a,
A.A. Aziz^c, R. Farma^a

^a School of Applied Physics, Faculty of Science and Technology, Universiti Kebangsaan Malaysia, 43600 Bangi, Selangor, Malaysia

^b H.E.J. Research Institute of Chemistry, International Centre for Chemical and Biological Sciences, University of Karachi, Karachi 75270, Pakistan

^c Malaysian Palm Oil Board, P.O. Box 10620, 50720 Kuala Lumpur, Malaysia

ARTICLE INFO

Article history:

Received 11 April 2013

Received in revised form

22 August 2013

Accepted 26 August 2013

Available online 17 September 2013

Keywords:

Elaeis guineensis

Heliotropium dasycarpum

Guaiacum officinale

Energy storage

Binderless composite electrodes

Porosity

ABSTRACT

Binderless composite monolith (BCM) electrodes prepared from carbon nanotubes (CNTs) and self-adhesive carbon grains (SACGs) were used in a symmetrical supercapacitor. The SACGs were prepared from fibers of oil palm empty fruit bunches (EFBs) from oil palm tree (*Elaeis guineensis*), *Heliotropium dasycarpum* (*H. dasycarpum*) and *Guaiacum officinale* (*G. officinale*). For each biomass, the BCMs were prepared by the carbonization and activation of green monoliths (GMs) containing SACGs treated with KOH and a mixture of SACGs and CNTs treated with KOH. Thermal decomposition behavior of all SACGs was found to be slightly different because of the difference in their compositions. In addition, BCMs from *H. dasycarpum* and *G. officinale* were found to have SiO₂. The BET surface areas were 1656, 1031 and 532 m² g⁻¹ for the BCMs from EFB, *H. dasycarpum* and *G. officinale*, respectively, and these values decreased by 40, 50 and 31% upon CNTs addition. Consequently, the specific capacitance decreased from ~124 to ~104 and ~49 F g⁻¹ to ~111, ~87 and ~31 F g⁻¹, respectively. However, addition of CNTs reduced the equivalent series resistance (ESR) by a factor of 83.9 (EFB), 90.6 (*H. dasycarpum*) and 38.8 (*G. officinale*) %. It was also found that CNTs addition contributed to improving the decay of C_{sp} with increasing scan rate if the electrode surface area was sufficiently high.

© 2013 Elsevier Ltd. All rights reserved.

1. Introduction

Supercapacitors, ultracapacitors or electric double layer capacitors (EDLCs), which consist of a pair of electrodes, an electrolyte and a pair of current collectors, store electrical energy in an electrochemical double layer formed at the

interface between the electrically charged surface of the electrode and the ionic charges of the electrolyte solution [1,2]. The value of capacitance is generally proportional to the specific area of the electrodes [3], but there have been many cases where capacitance deviated from this proportionality behavior [4]. Compared to conventional capacitors, the large

* Corresponding author.

E-mail addresses: madra@ukm.my, mderaman113@gmail.com (M. Deraman).
0959-6524/\$ – see front matter © 2013 Elsevier Ltd. All rights reserved.



electrode surface area in supercapacitors can generate large energy storage capability or high capacitance values (expressed in Farads) because large amounts of double layer are formed at the electrode-electrolyte interface and because the thickness of the double layers is very small (a few nanometer thickness depending on the diameter of the ion of the electrolyte solution used) [5].

Activated carbon electrodes have been widely used as electrode materials for supercapacitors because of their good physicochemical stability, high surface area, and well-developed pore-size distribution, which can be adapted to the size of the electrolyte ions [6,7]. Activated carbon produced from biomass materials has been known to be extremely porous because of interconnected cavities between pseudographitic layers. These layers result in a high internal surface area and are of great interest for application as supercapacitor electrodes [8,9]. Therefore, biomass materials such as wheat straw [10], rubber wood sawdust [11,12], waste tea leaves [13], chicken feathers [14], seaweed carbon [15], oil palm empty fruit bunches (EFB) [16,17], sunflower seed shell [18], corn grains [19], Neem dead leaves [20] and celtuce leaves [21] have been used as precursors to produce supercapacitor electrodes. In the present study, fibers of EFB from oil palm tree (*Elaeis guineensis*) from Malaysia [22], biomass residuals from medicinal extraction processes (three successive solvent extractions with methanol) of Pakistanis-flora (*Heliotropium dasycarpum*) [23] and Jamaican-flower (*Guaiacum officinale*) [24] were pre-carbonized and processed to produce activated carbon electrodes for supercapacitor applications. It is well known that highly porous activated carbon electrodes have very low electrical conductivity; to overcome this limitation, CNTs have been used as additives to reduce the electrical resistance of electrodes and improve the specific power of supercapacitors [16,25].

The advantages of using biomass (or their derivatives) include their high availability, relatively low cost, sustainable and renewable sources and reduced environmental impact if the biomass used is taken from waste generated by industrial activities. Biomass offers an alternative to the use of harmful chemical precursors and thus reduces hazards during the synthesis and post-processing of electrode materials [26,27]. Moreover, the utilization of biomass materials for fabricating electrode materials to be used for energy storage devices will help to minimize the use of fossil materials (coal and petroleum-based sources).

2. Materials and methods

2.1. Materials

2.1.1. EFBs from oil palm tree (*Elaeis guineensis*)

The fibers of EFBs were supplied by the Ecofibre Technology Sdn. Bhd. The properties of EFBs have been summarized elsewhere [22]. EFBs consist of fibers or bundles of fibers that are stringy and flexible. The mass fraction of fresh EFBs consist of 34% dry matter and 3% oil and 63% water and represents approximately 20–22% of the weight of fresh fruit bunches. EFBs contain a lignocellulosic natural polymer ma-

hemicellulose and 25–35% lignin. In the dry form, the mean mass fraction percentages of chemical composition are as follows: ash (6.3), oil (8.9), C (42.8), N₂ (0.8), P₂O₅ (0.22), K₂O (2.9), MgO (0.3) and CaO (0.25).

2.1.2. *Heliotropium dasycarpum* (*H. dasycarpum*)

H. dasycarpum is a heliotrope species that can be found worldwide, mainly in tropical and subtropical regions, including Kalat, Pakistan [28]. *H. dasycarpum* has been widely used for traditional medicine and biomedical research because it contains a 1.92% mass fraction (dry weight basis) of medicinal bioactive compounds [23]. All *H. dasycarpum* plant material obtained from Kalat, Pakistan was shade-dried and chopped, and its bioactive compound was extracted with methanol [29]. This treated and shade dried *H. dasycarpum* (1 kg) was supplied to our research group to be used as a precursor for the production of supercapacitor electrodes.

2.1.3. *Guaiacum officinale* (*G. officinale*)

G. officinale, known to be a source of pure lignum vitae, is commonly found in tropical areas, mainly in Central, North and South America and including the Caribbean islands [24]; additionally, it has been introduced and cultivated in Karachi, Pakistan [30]. *G. officinale* is a slow-growing, small to medium sized tree that reaches 3–10 m in height [24]. Wood from *G. officinale* is hard, heavy (oven dried density of 1050 kg m³), strong, long lasting, and it is known as an invaluable material for construction and wooden household products [24]. Its extract has historically been used as a herbal medicine to cure some diseases [24]. The bark of *G. officinale* plants cultivated on the premises of the University of Karachi was collected, air-dried, chopped and extracted with methanol, which was then concentrated under reduced pressure, to extract its medicinal bioactive compounds [30]. For the present study, the resulting treated and shade dried bark was used as a precursor to produce supercapacitor electrodes.

2.2. Electrode preparation and cell fabrication

Based on the procedure previously developed for fibers of EFBs [16], *H. dasycarpum* and *G. officinale* residues were converted to SACGs by low temperature pre-carbonization (~280 °C), grinding into a powder that passed through 300–500 µm hole size filters, 18 h of ball-milling and sieving to obtain SACGs up to 106 µm. Table 1 describes the SACGs prepared from EFB, H.

Table 1 – Mixture composition and labels for all tested samples.

Biomass	Mixture composition (%)			Green monolith	Binderless composite monolith
	SACG	KOH	CNT		
EFB	95 (SACG1)	5	0	GMK1	BCMK1
	90 (SACG1)	5	5	GMT1	BCMT1
<i>H. Dasycarpum</i>	95 (SACG2)	5	0	GMK2	BCMK2
	90 (SACG2)	5	5	GMT2	BCMT2
<i>G. Officinale</i>	95 (SACG3)	5	0	GMK3	BCMK3
	90 (SACG3)	5	5	GMT3	BCMT3



dasycarpum and *G. officinale*, labeled SACG1, SACG2 and SACG3, respectively. The SACGs from EFB, *H. dasycarpum* and *G. officinale*, and the mixtures of SACGs and CNTs were chemically treated with KOH (Table 1). The CNTs used in this study were 50–100 nm in diameter and 5–10 μm in length, with a surface area of approximately $40 \text{ m}^2 \text{ g}^{-1}$ (Nano Amor Nanostructured & Amorphous Materials, Inc., Texas, USA, manufactured on February 19th, 2009).

The green monoliths (GMs) were prepared by pressing 0.75 g of SACGs or mixtures of SACGs and CNTs in a 20 mm diameter mold at 250 kg cm^{-2} , and the respective labels are shown in Table 1. Based on the previous multi-step heating profile, the GMs were carbonized up to 800°C in a flow of $1.5 \text{ L min}^{-1} \text{ N}_2$ gas to produce the carbon monoliths [31]. The carbon monoliths were physically activated for 3 h at 800°C in a $1.0 \text{ L min}^{-1} \text{ CO}_2$ gas flow at a heating rate of 5°C min^{-1} to produce BCMs, and their respective labels are shown in Table 1. The BCMs were then polished to obtain a thickness of $400 \mu\text{m}$ and extensively washed with distilled water until reaching pH 7 before being used as electrodes in supercapacitor cells. The mass (m), thickness (t) and diameter (d) of the GMs and BCMs were measured, and their density was calculated from these data.

For investigation of the electrochemical properties of the BCMs, symmetrical supercapacitor cells were fabricated using the BCMs as their electrodes. The cell consisted of two BCM electrodes, two stainless steel current collectors (thickness $50 \mu\text{m}$) and an aqueous H_2SO_4 (1 mol L^{-1}) electrolyte occupying space between the BCM electrodes separated by a Teflon spacer (thickness $100 \mu\text{m}$).

2.3. Physical characterization

The thermal properties of SACGs were analyzed using Thermal Gravimetry (TG) and Differential Thermal Gravimetry (DTG) instruments (Mettler Toledo TGA/SDTS 851). The structure of the BCMs was investigated using an X-ray diffractometer (Bruker AXS D8) employing $\text{K}_\alpha \text{ Cu}$ radiation of 1.5406 \AA and scanning over the angular range 2θ from 0° to 70° . The morphological structures of the fractured BCMs were investigated using a field emission scanning electron microscope (FESEM) (Supra PV 55 model). Porosity of the BCMs was investigated by conducting N_2 adsorption–desorption isotherm measurements at 77 K using an accelerated surface area porosimeter system (ASAP 2020 Micromeritics). The porosity parameters, such as BET surface area (S_{BET}), surface area of micropores (S_{micro}), surface area of mesopores (S_{meso}), mesopore volume (V_{meso}), micropore volume (V_{micro}) and average pore diameter (D), were obtained from the N_2 adsorption–desorption isotherm data using ASAP 2020 software and the standard formalism.

2.4. Electrochemical characterization

The fabricated symmetrical supercapacitor cells were characterized using electrochemical impedance spectroscopy (EIS), cyclic voltammetry (CV) and galvanic charge-discharge (GCD) methods. The instruments used were a Solartron 1286 electrochemical interface and a Solartron 1255 HF frequency

electrode can be calculated using equation (1) through equation (3) from the EIS, CV and GCD data [32]

$$C_{\text{sp}} = \frac{1}{\pi f Z'' m} \quad (1)$$

$$C_{\text{sp}} = \frac{2i}{S m} \quad (2)$$

$$C_{\text{sp}} = -\frac{2i'}{m} \left(\frac{\Delta t}{\Delta V} \right) \quad (3)$$

where f is the lowest frequency, Z'' is the imaginary impedance at f , i is the electric current, S is the scan rate, ΔV is the voltage different, Δt is the discharge period, i' is the current density and m is the average mass of the electrodes.

The specific capacitance (C_{sp}) and its real (C') and imaginary (C'') parts are widely evaluated as a function of the frequency and can be calculated from the Nyquist plot produced by the EIS measurements using equations (4)–(6).

$$C_{\text{sp}} = \left\{ \left\{ (C'')^2 + (C')^2 \right\}^{1/2} \right\} / m \quad (4)$$

$$C' = -Z''(\omega) / \omega |Z(\omega)|^2 \quad (5)$$

$$C'' = -Z'(\omega) / \omega |Z(\omega)|^2 \quad (6)$$

where $Z'(\omega)$ is the real impedance, $Z''(\omega)$ is the imaginary impedance, $C(\omega) = C'(\omega) - jC''(\omega)$, and $Z(\omega) = 1/j\omega C(\omega)$ [33].

The specific power and specific energy were calculated from the GCD data using equations (7) and (8), respectively

$$P = \frac{Vi}{m} \quad (7)$$

$$E = \frac{Vit}{m} \quad (8)$$

where V is the voltage, i is the current and t is the time.

3. Results and discussion

3.1. Physical properties

The thermal properties of the SACG residues were investigated over the temperature range of 20°C – 600°C , and the TG and DTG data are shown in Fig. 1. As seen, all of the SACGs exhibited a slight weight loss of approximately 10% with a distinctly increasing rate of weight loss at temperatures of 30°C – 100°C , corresponding to the release of moisture and water evaporation [34,35]. The decomposition of other volatiles began at approximately 250°C , and the most weight lost (approximately 50%) occurred between 250°C and 380°C . This thermal decomposition behavior is typical for most biomass materials and is associated with the decomposition of hemicelluloses, cellulose and lignin from the samples [36]. Specifically, hemicelluloses begin to decompose at the lower end of this temperature range, followed by cellulose and lignin decomposition at slightly higher temperatures. For SACG1, the maximum rate of weight lost was higher and occurred at a lower temperature than SACG2 and SACG3, indicating that the

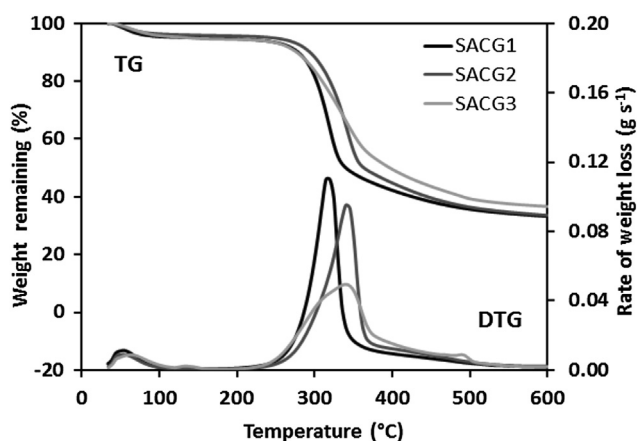


Fig. 1 – TG and DTG curves of self-adhesive carbon grains (SACGs) from biomass residues.

SACGs from different types of biomass materials exhibited different thermal decomposition behaviors. This behavior was evidence of the existence of slight variations in their chemical structures and compositional ratios. Furthermore, the yields for SACG1, SACG2 and SACG3 at 600 °C were 33.26%, 33.59% and 36.66%, respectively. For SACG3, the peak weight loss rate was broader because it was a combination of two peaks. The DTG results suggest that the peak weight loss rate for SACG3 (approximately 350 °C) was broader because it was a combination of two peaks associated with the decomposition of hemicellulose at approximately 310 °C (lower left peak) and the 355 °C (upper right peak). The absence of double peaks in the DTG results for SACG1 and SACG2 indicate that the hemicelluloses of the EFB and *H. dasycarpum* were completely decomposed during the pre-carbonization process.

Table 2 shows the mass (m), diameter (d), thickness (t) and density (ρ) of the GMs and BCMs for all samples. The yields of carbon electrodes prepared from GMs were estimated based on the data in Table 2. The yields of carbon electrodes prepared from GMs without and with CNTs were 26–32% and 35–40%, respectively. As seen in Table 2, the m , d and t values for all GMs samples were almost identical and gave rise to

almost identical ρ values. However, the density of the BCMK3 (or BCMT3) increased by 36.57% (or 40.26%) from their respective GMs, whereas the BCMK1 (or BCMT1) and BCMK2 (or BCMT2) decreased by 1.74% (or 0.45%) and 11.81% (or 10.73%), respectively. A slight increase (3.69%) in the ρ value due to CNTs was observed for precursor 3, while the ρ value decreased by 1.29% and 1.08% for precursors 1 and 2, respectively, due to CNTs. The change in ρ is different between the electrodes (with or without CNTs) from precursor 3 and the electrodes (with or without CNTs) from precursor 1 and precursor 2. This result is because precursor 3 has a different morphology and a higher degree of molecular cross-linking compared to the other precursors. The density, hardness and porosity of the carbonized products are influenced by these properties because the mechanisms of releasing non-carbon substances from the samples and the rearrangement of the carbon atoms to form turbostratic structures are dependent on the precursors properties during carbonization and activation. The morphology and molecular cross-linking of precursor 3 suggest advantages over precursor 1 and precursor 2, as indicated by the higher density of GMs and BCMs. Therefore, during the polishing of the BCMs, it was noticed that BCM3 was tougher and harder to polish compared to BCM1 and BCM2. This behavior is consistent with the density data presented in Table 2.

Fig. 2 shows the X-ray diffractograms for all BCMs. The structure of all BCMs was semicrystalline as evidently shown by the presence of two broad peaks due to (002) and (100) diffraction planes at 2θ approximately 25° and 41.6°, respectively. These broad signals showed that the BCMs from all precursors have turbostratic structure; similar results were reported previously for the BCMs from EFB [37]. The sharp peak at $2\theta \sim 26.6^\circ$ apparent in the diffractograms is attributed to the presence of crystalline SiO_2 in the samples, which was confirmed by the detection of Si using an energy dispersive x-ray analysis (EDAX) measurement.

The micrographs of the BCMs fractured surfaces obtained by FESEM at a magnification of 50k \times are shown in Fig. 3. The obvious differences in microstructure between the BCMK and BCMT samples were clear. The presence of CNTs in the latter samples in the micrographs appeared as cylindrical shapes similar to those reported by others [5,38]. CNTs seemed to

Table 2 – Mass (m), dimension (diameter, d and thickness, t) and density (ρ) of the green monoliths (GMs) and binderless carbon monoliths (BCM).s).

Samples	m (g)	d (mm)	t (mm)	ρ (g cm $^{-3}$)
GMK1	0.7381	2.3097	20.22	0.9957
GMK2	0.7381	2.3547	20.30	0.9692
GMK3	0.7323	2.1630	20.20	1.0566
BCM1	0.2359	1.5317	14.13	0.9784
BCM2	0.1943	1.5507	13.60	0.8547
BCM3	0.2297	1.3052	12.53	1.4430
GMT1	0.7431	2.2490	20.14	1.0377
GMT2	0.7379	2.3103	20.19	0.9999
GMT3	0.7340	2.1210	20.13	1.0880
BCMT1	0.2946	1.6613	15.04	0.9914
BCMT2	0.2603	1.6830	14.79	0.8918
BCMT3	0.2718	1.3178	12.57	1.5566

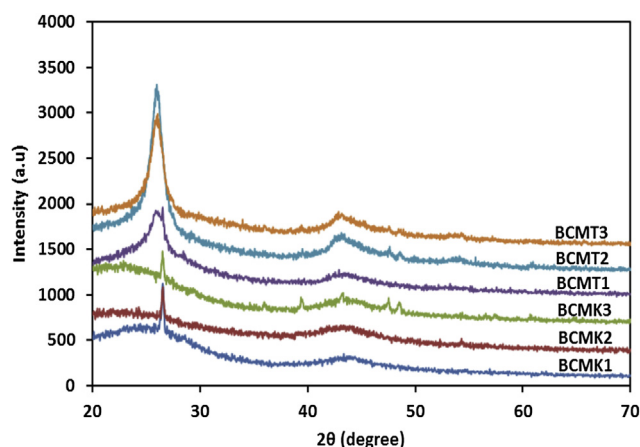


Fig. 2 – X-ray diffractograms for all BCMs.

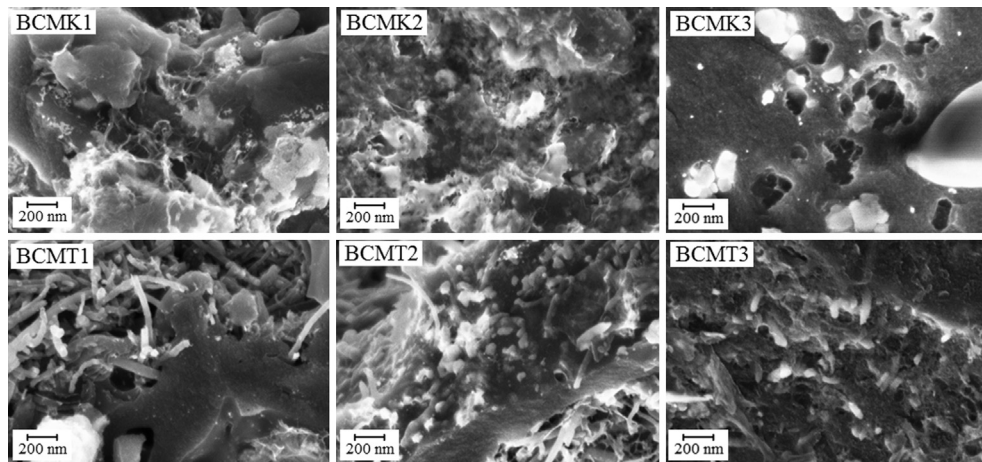


Fig. 3 – FESEM micrographs for all BCMS.

uniformly disperse and occupy the pores of each material, thus directly affecting the porosity of the samples. The pores in these three materials were well distributed, but BCMK3 appeared to have less pores.

The porosity of the BCMS was investigated using N_2 adsorption–desorption isotherms (Fig. 4). Based on IUPAC data classification, the isotherm profiles for all BCMS exhibited type IV patterns, similarly found in activated carbon from rubber wood sawdust and seaweed carbons [11,15]. This type represents the combination of microporous and mesoporous pore structures. The low P/P_0 region was associated with monolayer-multilayer adsorption on the mesopore walls, while the high P/P_0 region was associated with limited uptake and capillary condensation [39,40].

The S_{BET} , S_{meso} , S_{micro} , V_{meso} , V_{micro} and D calculated from the isotherms data are shown in Table 3. The results in this table clearly show that the S_{BET} was highest for BCMK1, followed consecutively, which included micropores and mesopores parameters, by a significant decrease for BCMK2 and BCMK3. This trend was maintained by the BCMS with CNTs, but a significant decrease of surface area due to CNTs addition was revealed by the data. The largest decrease was for sample

2 (50%), followed by sample 1 (40%) and sample 3 (31%). These values indicated a significant effect of CNTs on the pore characteristics of the electrodes, which could result from the occupation of CNT particles in some pores or the inhibition of pore formation during carbonization and activation due to the presence of CNTs in GMs. Another notable trend in Table 3 was that the S_{meso} (or V_{meso}) was higher than the S_{micro} (or V_{micro}), which was expected because the hysteresis loops in Fig. 4 were very pronounced. Furthermore, the D values were found to increase with the addition of CNTs. This increase indicated that the CNTs caused pore widening during the carbonization and activation processes.

3.2. Electrochemical properties

3.2.1. Electrochemical impedance spectroscopy

EIS curves (impedance data) over a frequency range of 10 mHz–1 MHz for all BCMKs and BCMTs cells in Fig. 5 (a) exhibited typical frequency-dependent behavior of the Nyquist plot for carbon-based supercapacitors, depending on the frequency region. In the high frequency region, there was a relatively small semicircle representing the dominant resistive nature of the supercapacitor electrode/electrolyte/current-collector system. In the middle frequency region, there was a segment of a straight line with a slope of approximately 45° , which represented the combination of resistive and capacitive behaviors for the ions penetrating into

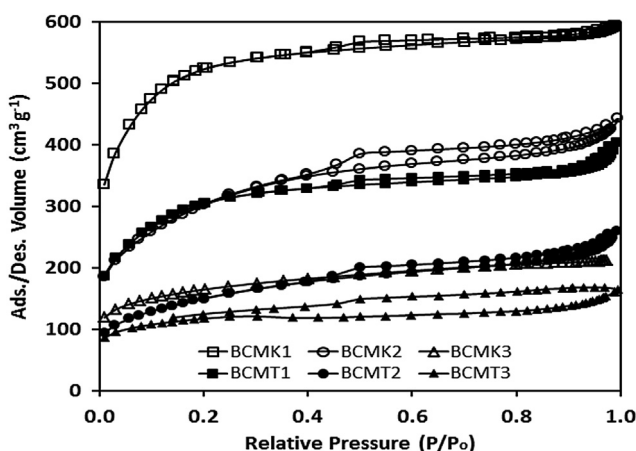


Table 3 – Porosity parameters obtained from N_2 adsorption–desorption isotherm data for all of the BCMS.

Sample	S_{BET} ($m^2 g^{-1}$)	S_{meso} ($m^2 g^{-1}$)	S_{micro} ($m^2 g^{-1}$)	V_{meso} ($cm^3 g^{-1}$)	V_{micro} ($cm^3 g^{-1}$)	D (Å)
BCMCK1	1655.49	1010.94	644.54	0.3002	0.3645	22.04
BCMCK2	1030.82	911.01	119.81	0.4757	0.0676	25.57
BCMCK3	532.37	317.18	215.18	0.3297	0.1155	24.78
BCMT1	993.79	795.32	198.47	0.3265	0.1217	24.09
BCMT2	514.89	450.01	64.88	0.3124	0.0352	29.90
BCMT3	368.66	206.76	161.90	0.1191	0.9044	26.83

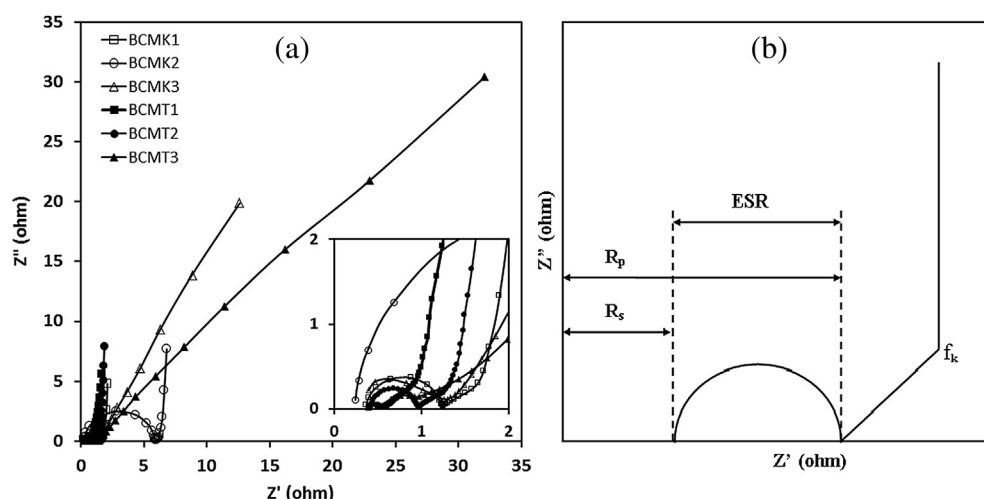


Fig. 5 – (a) Nyquist plots and (b) schematic Nyquist plots for all BCMs cells.

the electrode pores. In the low frequency region, there was a segment of a sharply increasing straight line that represented the dominance of capacitive behavior from the formation of ionic and electronic charges in the electric double layer system at the micropore surfaces. At this frequency, the ions could more easily diffuse into the micropores [11].

The curve for each cell shown in Fig. 5 (a) had a similar general shape with a difference in their detail behavior due to the difference in the pore characteristics of their electrodes. The detail differences were conveniently distinguished by analyzing these curves in terms of the parameters shown in Fig. 5 (b). The parameters were R_s , the resistance of the electrolyte and the contact resistance between the current collector and electrode, R_p , the internal resistance of the electrode, the diameter of the semicircle, $R_p - R_s$, which is equal to the ESR (equivalent series resistance) value of the cell, and f_k , the knee frequency, which is an initiation point of the dominant supercapacitive segment line in relation to its resistance, $R_k = Z'_k$.

The values of R_s , R_p , ESR and f_k for all the cells determined from the data in Fig. 5 (a) are listed in Table 4. The R_s values were small (less than 1 Ω) and typical for supercapacitors using H_2SO_4 as their electrolyte. A small difference in the R_s values was due to the variation in the contact resistance between the current collector and the electrode. These values of R_s were comparable with those reported in the literature, which ranged from 0.50 to 2.00 Ω for carbon from wheat straw

[10], 0.49 to 0.55 Ω for carbon from rubber wood sawdust [11], and 0.74 to 0.78 Ω for carbon from waste tea leaves [13]. CNTs seemed to increase the R_s values, supporting their effect on the contact resistance between current collector and electrode. The R_p values appeared to vary with the electrode type and led to a notable difference in the ESR values of the cells. The ability of CNTs to reduce the ESR values is clearly shown in Table 4 for all types of electrodes. Comparison between the ESR values of the BCMT cells showed that these ESR values decreased with decreasing surface area of their respective electrodes. These behaviors have also been observed in recent studies on supercapacitors using other carbon precursors, which reported ESR values of 2.28 Ω , 0.97 Ω and 0.43 Ω for surface areas of 2126, 1911 and 1839 $m^2 g^{-1}$, respectively [14]. The reduction in the ESR values was not solely due to the change in surface area but also arose from the increase in the electronic conductivity of the electrode upon addition of CNTs [41].

Another trend that resulted from the addition of CNTs was that for all three types of electrodes, the supercapacitive line of the BCMT cell was positioned at a lower Z' value than its respective BCMK cell. A similar trend was observed in another recent study [42]. Furthermore, CNTs also increased the Z'' value at the lowest frequency and hence decreased the C_{sp} because it is inversely proportional to Z'' . The values of C_{sp} calculated from the EIS data using equation (1) are shown in Table 5. As seen, the C_{sp} results for the BCMK cells showed a decreasing trend and were consistent with the decreasing surface area data shown in Table 3. The same trend was observed for the BCMT cells, but with slightly lower values of C_{sp} . A similar reduction in the C_{sp} values by CNTs was also observed in other studies (i.e., 95 $F g^{-1}$ and 90 $F g^{-1}$ for cells using carbon electrodes without and with CNTs, respectively) [43].

Fig. 5 (a) also shows that the supercapacitive lines for BCMK3 were significantly less vertical than type 1 and 2 cells. This decrease in verticalness was a consequence of the significantly lower surface area possessed by the electrodes in this cell (Table 3). Addition of CNTs caused supercapacitive

Table 4 – R_s , R_p , ESR and f_k for all of the BCM cells.

Cell	$R_s(\Omega)$	$R_p(\Omega)$	ESR(Ω)	$f_k(Hz)$
BCMCK1	0.35	1.24	0.89	0.32
BCMCK2	0.21	5.90	5.74	0.63
BCMCK3	0.36	1.27	0.93	—
BCMT1	0.39	0.54	0.14	0.25
BCMT2	0.41	0.95	0.54	—

Table 5 – Specific capacitance (C_{sp}), specific power (P), specific energy (E) and ratios of S_{meso}/S_{micro} for the tested cells.

Cell	$C_{sp}(\text{F g}^{-1})$			$E (\text{Wh kg}^{-1})$ (GCD)	$P (\text{W kg}^{-1})$ (GCD)	S_{meso}/S_{micro}
	EIS	CV	GCD			
BCMK1	111	128.77	133	3.82	158	1.57
BCMK2	94	108.89	109	2.55	198	7.60
BCMK3	23	98.80	25	0.43	134	1.47
BCMT1	95	117.12	121	3.54	160	4.00
BCMT2	73	102.57	85	2.53	173	6.94
BCMT3	15	68.22	10	0.17	133	1.28

cell performance to decrease because its slope decreased and length increased (BCMT3 cell), which was consistent with a further decrease in surface area of its electrodes (Table 3). It will be seen in a later section that these inferior pore characteristics of the type 3 electrodes affected the power and energy performance of the cells. These results suggested that the addition of the CNTs would only be beneficial provided that the surface area of the electrode was sufficient, as has been observed elsewhere [32]. Contrary to the case of type 2 electrodes which possessed surface area sufficiently higher; thus, addition of CNTs contributed significantly to reducing the ESR from 5.74 to 0.54 Ω (Table 4).

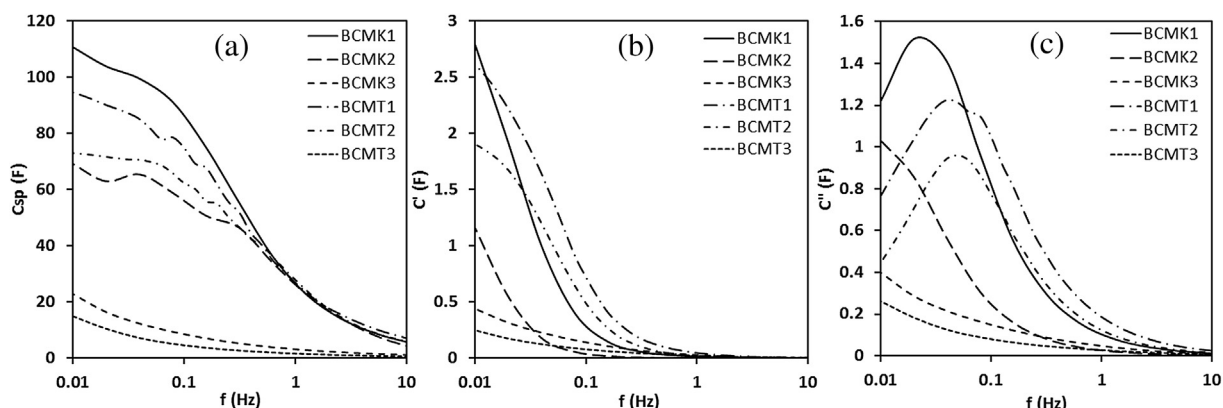
Ideal Warburg lines have a slope gradient of approximately 45° [44]. Except for the BCMK1 cell, the slope and length of the Warburg line for the other cells are shown in Fig. 5 (a). Interestingly, their slope gradients were all lower than 45° . The length of the Warburg line seemed to change slightly with respect to electrode type and CNTs addition. It is well known that a higher slope gradient and a shorter Warburg line are associated with a better supercapacitive characteristic of a cell. For electrode types 1 and 2, addition of CNTs increased the slope gradient by a factor of 27 and 9.3%, respectively. For electrodes of type 3, the Warburg line only appeared after the addition of CNTs. These results demonstrated that CNTs affected the mobility of electrolyte ions entering into pores of electrodes in this intermediate frequency region and that the extent of such an effect depended on the pore characteristic of the carbon matrix. Examination of electrolyte ion mobility in porous electrodes in the Warburg frequency region was

performed for supercapacitors using CNTs and carbon electrodes from CNTs and activated carbon materials [44].

Fig. 6 (a), (b) and (c) shows the specific capacitance and real (C') and imaginary (C'') capacitance of the BCM cells calculated using equations (4)–(6), respectively, as a function of frequency. In Fig. 6 (a), the C_{sp} strongly depended on the frequency below 1 Hz, particularly for the BCMK cells, which showed a higher C_{sp} throughout the frequency region. A similar frequency dependence was also exhibited by the C' and C'' curves in Fig. 6 (b) and (c). For the C'' curve, there is a peak frequency value (f_p). This frequency value is associated with the relaxation time constant, τ_o , which defines the boundary between the regions of capacitive and resistive behaviors for a supercapacitor. It is well known that higher power delivery corresponds to lower τ_o values. Based on the f_p values in Fig. 6 (c), the value of τ_o was estimated using the equation $\tau_o = 1/f_p$. The results obtained were 3.16, 1.58 and 3.98 s for the BCMK1, BCMK2 and BCMT1 cells, respectively. The τ_o values for the other cells could not be calculated because the peaks fell below the detection limit of the instrument.

3.2.2. Cyclic voltammetry

The cyclic voltammograms, recorded at a scan rate of 1 mV s^{-1} within the potential range of 0.1–1.0 V for all the investigated cells, are shown in Fig. 7. All voltammograms for cells 1 and 2 had symmetrical rectangular shapes representing a common supercapacitive characteristic for a carbon-based symmetrical supercapacitor. These plots were evidence that these cells had good reversibility and high EDLC stability during charge and discharge. This superior performance resulted from significant EDLC formation in the pores of the electrodes occupied by 1 M H_2SO_4 electrolyte during the energy storage process [3,45]. Cells 1 and 2 also exhibited broader voltammogram areas, indicating that they were superior to the other types of cells. For cell 3, the voltammogram exhibited a relatively smaller window area, and the shape notably deviated from the typical rectangular shape. Unlike cells 1 and 2, at switching potentials (~ 0.1 and ~ 1.0 V), the rapid current response of cell 3 to voltage diminished. This behavior indicated an inferior performance for cell 3 due to the lack of fast ion transport in the EDLC system [38,45]. The C_{sp} values calculated using equation (2) based on the data in Fig. 7 are



and (b) real and (c) imaginary capacitance for the BCM cells.

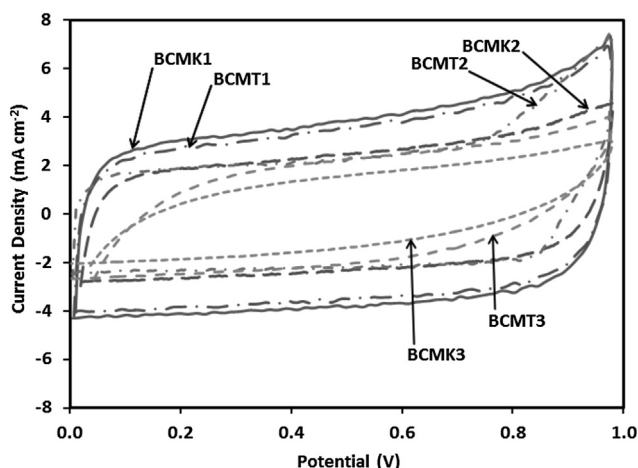


Fig. 7 – Cyclic voltammograms for the BCM cells.

listed in Table 5 and clearly show that these results were consistent with EIS and CV results.

For electrode type 1, the addition of CNTs decreased C_{sp} at a lower scan rate and increased C_{sp} at a higher scan rate (Fig. 8). For electrode type 2, C_{sp} improved significantly upon addition of CNTs for all scan rate regions. In contrast to the two other electrodes, addition of CNTs to electrode type 3 enhanced the decay of C_{sp} . At the scan rate of 100 mV s^{-1} , the C_{sp} for electrodes type 1 and type 2 with CNTs remained higher, with only 59% and 53% decay, respectively, compared to 76% and 93% decay without CNTs. Similar trends were observed in a study involving the addition of CNTs to activated electrodes prepared from fibers of EFB [46].

3.2.3. Galvanostatic charge–discharge

The GCD curves recorded at a current density of 0.1 mA cm^{-2} over a voltage range of 0.01–1.00 V for all the investigated cells are shown in Fig. 9. Each curve exhibited a similar isosceles triangular shape with charge and discharge potentials varied linearly with time. These shapes indicated that all cells exhibited supercapacitive behavior. However, the area under the triangle, which represents the capacitive level of the cells,

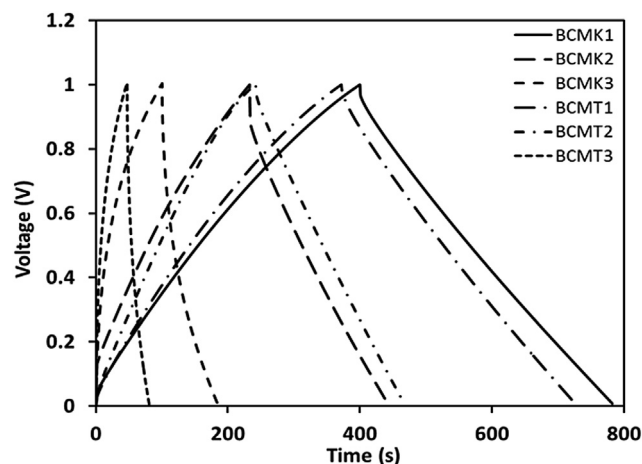
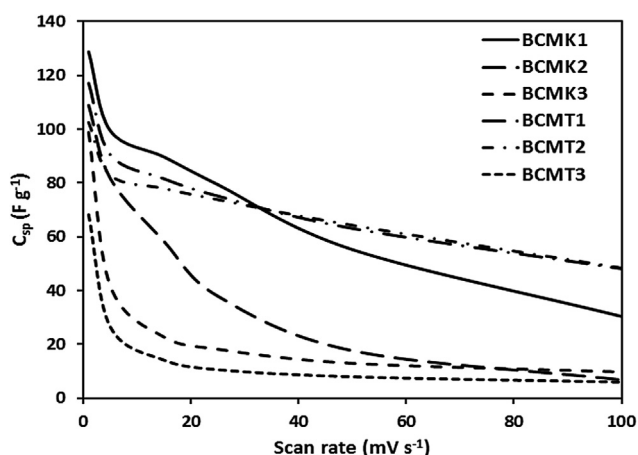


Fig. 9 – GCD curves at 10 mA cm^{-2} current density for all BCM cells.

varied with the type of electrode used. The triangular area was broader for the BCMK1 cell and was decreased for the BCMK2 and BCMK3 cells. Addition of CNTs further reduced the triangular area for all of the BCMT cells. A clear difference in the supercapacitive behavior between cells was observed in the C_{sp} values calculated from the GCD curves in Fig. 9 using equation (3). The specific C_{sp} values are listed in Table 5, and the trend of these values was in good agreement with the EIS and CV methods.

A slight voltage drop at the beginning of the discharge curve appeared in all GCD curves in Fig. 9. This drop was associated with the ESR of the cells, which could be calculated using $\text{ESR} = iR_{\text{drop}}/2I$, where iR_{drop} is defined as the electrical potential difference at the beginning of the discharge curves, and I is the discharge current [47]. The calculated ESR values for the BCMK1, BCMK2 and BCMK3 cells were 1.68, 5.94 and 2.75Ω , respectively. Addition of CNTs was found to decrease the ESR values of the cells to 0.99, 1.54 and 2.44Ω for the BCMT1, BCMT2 and BCMT3 cells, respectively. A similar decrease in the ESR values by CNTs was observed in the study of supercapacitors using porous carbon electrodes containing CNTs (i.e., from 0.5 to 0.38Ω in Ref. [43] and from 45 to 2.5Ω in Ref. [48]). The reduced ESR values could improve the power performance of the cells because the power is inversely proportional to ESR.

3.2.4. Ragone plots (specific power against specific energy)

The specific power (P) and specific energy (E) of the cells, calculated from the GCD discharge curves in Fig. 9 using equations (7) and (8), respectively, are presented as Ragone plots in Fig. 10. All P – E plots in this figure showed a typical pattern of decrease in power as energy increased for carbon-based supercapacitors. The BCMK3 cell demonstrated a significantly poorer P – E relationship performance than the other cells based on electrodes of type 1 and 2, i.e., its maximum P and E were smaller. This poorer performance was enhanced by the addition of CNTs (BCMT3 cell). For the BCMK2 cell, its maximum P value was the highest but decreased faster within a lower and narrower E range compared to that of the BCMK1 cell. The effect of CNT addition was significantly

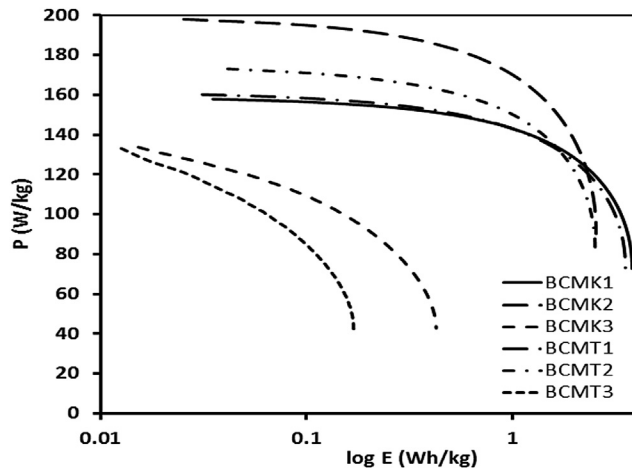


Fig. 10 – Specific power against specific energy, or Ragone plots, for all BCM cells.

greater for electrode type 2, particularly in the low E region. In contrast, electrode type 1 was significantly affected by CNT addition only in the high E region. These features were strongly correlated with the pore characteristics of the electrodes of the cells. To observe this correlation, Table 5 relates the electrode pore characteristics ($S_{\text{meso}}/S_{\text{micro}}$) to their corresponding P – E patterns for the present work and other data reported in the literature. For comparison, Table 6 lists the specific capacitance and surface area of electrodes prepared from different precursors.

4. Conclusions

From this study, the following conclusions could be made: (i) the type of precursor strongly influences the pore characteristic and electrochemical behavior of the electrodes, (ii) the

addition of CNTs significantly affects the pore characteristic and electrochemical behavior of the electrodes, (iii) the addition of CNTs is only beneficial if the electrode has significantly higher surface area, (iv) the self-adhesive property of SACGs prepared from biomass eliminates the need for a binder in preparing electrodes in a monolithic form, (v) SACGs are compatible with a high degree of reliability in mixing with CNTs for the modification of electrode performance, and (vi) the performances of electrodes from EFB and *H. dasycarpum* are comparable to those of electrodes prepared from other types of biomass precursors reported in the literature.

Acknowledgments

The authors are grateful to the UKM research grants UKM-DLP-2012-022, UKM-DLP-2012-023, ERGS/1/2012/STG05/UKM/01/2 and UKM-Industri-2013-026 for financial support of this project. We would also like to acknowledge the Research Institute of Chemistry, International Centre for Chemical and Biological Sciences, University of Karachi, Karachi, Pakistan for the gift of materials, comments from Dr. Farrukh Mansoor, and the instruments provided by CRIM, UKM.

REFERENCES

- [1] Elmouwahidi A, Zapata-Benabith Z, Carrasco-Marín F, Moreno-Castilla C. Activated carbons from KOH-activation of argan (*Argania spinosa*) seed shells as supercapacitor electrodes. *Bioresour Technol* 2012;111:185–90.
- [2] Olivares-Marín M, Fernández JA, Lázaro MJ, Fernández-González C, Macías-García A, Gómez-Serrano V, et al. Cherry stones as precursor of activated carbons for supercapacitors. *Mater Chem Phys* 2009;114(2):323–7.
- [3] Ismanto AE, Wang S, Soetaredjo FE, Ismadji S. Preparation of capacitor's electrode from cassava peel waste. *Bioresour Technol* 2010;101(10):3534–40.
- [4] Aworn A, Thiravetyan P, Nakbanpote W. Preparation of CO₂ activated carbon from corn cob for monoethylene glycol adsorption. *Colloids Surf A* 2009;333(1–3):19–25.
- [5] Kim J-I, Rhee K-Y, Park S-J. Interactive effects of pore size control and carbonization temperatures on supercapacitive behaviors of porous carbon/carbon nanotube composites. *J Colloid Interface Sci* 2012;377(1):307–12.
- [6] Pandolfo AG, Hollenkamp AF. Carbon properties and their role in supercapacitors. *J Power Sources* 2006;157(1):11–27.
- [7] Zhang LL, Zhao XS. Carbon-based materials as supercapacitor electrodes. *Chem Soc Rev* 2009;38(9):2520–31.
- [8] Ioannidou O, Zabaniotou A. Agricultural residues as precursors for activated carbon production—a review. *J Renew Sustain Energy* 2007;11(9):1966–2005.
- [9] Doble G, Dizhbite T, Gil MV, Volperts A, Centeno TA. Production of nanoporous carbons from wood processing wastes and their use in supercapacitors and CO₂ capture. *Biomass Bioenergy* 2012;46:1–10.
- [10] Li X, Han C, Chen X, Shi C. Preparation and performance of straw based activated carbon for supercapacitor in non-aqueous electrolytes. *Microporous Mesoporous Mater* 2010;131(1–3):303–9.
- [11] Taer E, Deraman M, Talib IA, Awitdrus A, Hashmi SA, Umar AA. Preparation of a highly porous binderless activated carbon monolith from rubber wood sawdust by a multi-step

Table 6 – Specific capacitance and surface area of electrodes made from various precursors.

Biomass precursor	S_{BET} ($\text{m}^2 \text{g}^{-1}$)	C_{sp} (F g^{-1})	Reference
Wheat straw	2312	251	[10]
Rubber wood sawdust	912	138	[11,12]
Waste tea leaves	2841	330	[13]
Chicken feather	1839	302	[14]
Seaweed	1082	170	[15]
Oil palm empty fruit bunches	1704	149	[16,17]
Sunflower seed shell	2509	311	[18]
Corn grains	3199	257	[19]
Neem (<i>Azadirachta indica</i>) dead leaves	1230	400	[20]
Celtuce leaves	3404	273	[21]
Oil palm empty fruit bunches	1656	110	Present study
<i>Heliotropium dasycarpum</i>	1031	109	Present study

- activation process for application in supercapacitors. *Int J Electrochem Sci* 2011;6:3301–15.
- [12] Taer E, Deraman M, Talib IA, Hashmi SA, Umar AA. Growth of platinum nanoparticles on stainless steel 316L current collectors to improve carbon-based supercapacitor performance. *Electrochim Acta* 2011;56(27):10217–22.
 - [13] Peng C, Yan X, Wang R, Lang J, Ou Y, Xue Q. Promising activated carbons derived from waste tea-leaves and their application in high performance supercapacitors electrodes. *Electrochim Acta* 2013;87:401–8.
 - [14] Wang Q, Cao Q, Wang X, Jing B, Kuang H, Zhou L. A high-capacity carbon prepared from renewable chicken feather biopolymer for supercapacitors. *J Power Sources* 2013;225:101–7.
 - [15] Bichat MP, Raymundo-Piñero E, Béguin F. High voltage supercapacitor built with seaweed carbons in neutral aqueous electrolyte. *Carbon* 2010;48(15):4351–61.
 - [16] Farma R, Deraman M, Talib IA, Omar R, Manjunatha JG, Ishak MM. Physical and electrochemical properties of supercapacitor electrodes derived from carbon nanotube and biomass carbon. *Int J Electrochem Sci* 2013;8:257–73.
 - [17] Farma R, Deraman M, Awitdrus A, Talib IA, Taer E, Basri NH. Preparation of highly porous binderless activated carbon electrodes from fibres of oil palm empty fruit bunches for application in supercapacitors. *Bioresour Technol* 2013;132:254–61.
 - [18] Li X, Xing W, Zhuo S, Zhou J, Li F, Qiao S-Z, et al. Preparation of capacitor's electrode from sunflower seed shell. *Bioresour Technol* 2011;102(2):1118–23.
 - [19] Balathanigaimani MS, Shim W-G, Lee M-J, Kim C, Lee J-W, Moon H. Highly porous electrodes from novel corn grains-based activated carbons for electrical double layer capacitors. *Electrochem Commun* 2008;10(6):868–71.
 - [20] Biswal M, Banerjee A, Deo M, Ogale S. From dead leaves to high energy density supercapacitors. *Energy Environ Sci* 2013;6(4):1249.
 - [21] Wang R, Wang P, Yan X, Lang J, Peng C, Xue Q. Promising porous carbon derived from celtuce leaves with outstanding supercapacitance and CO₂ capture performance. *ACS Appl Mater Interfaces* 2012;4(11):5800–6.
 - [22] Deraman M. Resistivity of carbon from oil palm bunches: percolation theory. *J Phys D Appl Phys* 1994;27:1060–2.
 - [23] Kurbanov D, Yunusov S Yu. Alkaloids of *Haplophyllum*. *Chem Nat Compd* 1967;3:244–5.
 - [24] Francis JK, Service UF. *Guaiacum officinale* L. *Lignumvitae*, Guayacán, Zygophyllaceae, Caltrop family. USDA Forest Service International Institute of Tropical Forestry Publications; 1993. SO-ITF-SM-67: 1–4.
 - [25] Zheng C, Qian W, Wei F. Integrating carbon nanotube into activated carbon matrix for improving the performance of supercapacitor. *Mater Sci Eng B* 2012;177(13):1138–43.
 - [26] Rufford TE, Hulicova-Jurcakova D, Zhu Z, Lu GQ. Nanoporous carbon electrode from waste coffee beans for high performance supercapacitors. *Electrochem Commun* 2008;10(10):1594–7.
 - [27] Garcia BB, Candelaria SL, Liu D, Sepheri S, Cruz JA, Cao G. High performance high-purity sol-gel derived carbon supercapacitors from renewable sources. *Renew Energy* 2011;36(6):1788–94.
 - [28] Ahmad M, Zafar M. Indigenous knowledge of folk medicine by The Women of Kalat and Khuzdar Regions of Balochistan, Pakistan. *Pak J Bot* 2010;42(3):1465–85.
 - [29] Firdous S, Ansari NH, Fatima I, Malik A, Afza N, Iqbal L, et al. Ophiomides A-B, new potent urease inhibitory sphingolipids from *Heliotropium ophioglossum*. *Arch Pharmacol Res* 2012;35(7):1133–7.
 - [30] Saba N, Khatoon R, Ali Z, Ahmad VU. A new Bidesmoside Saponin from the Bark of *Guaiacum officinale*. *J Chem Soc* 2012;2012(24):2400–4.
 - [31] Deraman M, Omar R, Zakaria S, Mustapa IR, Talib M, Alias N. Electrical and mechanical properties of carbon pellets from acid (HNO₃) treated self-adhesive carbon grain from oil palm empty fruit bunch. *J Mater Sci* 2002;7:3329–35.
 - [32] Portet C, Taberna PL, Simon P, Flahaut E, Laberty-Robert C. High power density electrodes for carbon supercapacitor applications. *Electrochim Acta* 2005;50(20):4174–81.
 - [33] Portet C, Yushin G, Gogotsi Y. Electrochemical performance of carbon onions, nanodiamonds, carbon black and multiwalled nanotubes in electrical double layer capacitors. *Carbon* 2007;45(13):2511–8.
 - [34] Zhang J, Gong L, Sun K, Jiang J, Zhang X. Preparation of activated carbon from waste *Camellia oleifera* shell for supercapacitor application. *J Solid State Electrochem* 2012;16(6):2179–86.
 - [35] Chunlan L, Shaoping X, Yixiong G, Shuqin L, Changhou L. Effect of pre-carbonization of petroleum cokes on chemical activation process with KOH. *Carbon* 2005;43(11):2295–301.
 - [36] Deraman M, Zakaria S, Omar R, Astimar AA. Electrical conductivity of carbon pellets from mixtures of pyropolymer from oil palm bunch and cotton cellulose. *Jpn J Appl Phys* 2000;39:L1236–8.
 - [37] Awitdrus, Deraman M, Talib IA, Omar R, Jumali MHH, Taer E, et al. Microcrystallite dimension and total active surface area of carbon electrode from mixtures of pre-carbonized oil palm empty fruit bunches and green petroleum cokes. *Sains Malays* 2010;39:83–6.
 - [38] Lee J-K, Pathan HM, Jung K-D, Joo O-S. Electrochemical capacitance of nanocomposite films formed by loading carbon nanotubes with ruthenium oxide. *J Power Sources* 2006;159(2):1527–31.
 - [39] Schneider P. Adsorption isotherms of microporous-mesoporous solids revisited. *Appl Catal A* 1995;129(2):157–65.
 - [40] Ryu Z, Zheng J, Wang M, Zhang B. Characterization of pore size distributions on carbonaceous adsorbents by DFT. *Carbon* 1999;37(8):1257–64.
 - [41] Inagaki M, Konno H, Tanaike O. Carbon materials for electrochemical capacitors. *J Power Sources* 2010;195(24):7880–903.
 - [42] Huang C-W, Chuang C-M, Ting J-M, Teng H. Significantly enhanced charge conduction in electric double layer capacitors using carbon nanotube-grafted activated carbon electrodes. *J Power Sources* 2008;183(1):406–10.
 - [43] Portet C, Taberna PL, Simon P, Flahaut E. Influence of carbon nanotubes addition on carbon-carbon supercapacitor performances in organic electrolyte. *J Power Sources* 2005;139(1–2):371–8.
 - [44] Emmenegger C, Mauron P, Sudan P, Wenger P, Hermann V, Gallay R, et al. Investigation of electrochemical double-layer (ECDL) capacitors electrodes based on carbon nanotubes and activated carbon materials. *J Power Sources* 2003;124(1):321–9.
 - [45] He X, Jiang L, Yan S, Lei J, Zheng M, Shui H. Direct synthesis of porous carbon nanotubes and its performance as conducting material of supercapacitor electrode. *Diamond Relat Mater* 2008;17(6):993–8.
 - [46] Farma R, Deraman M, Omar R, Awitdrus, Mohamad Ishak M, Taer E, et al. Binderless composite electrode monolith from carbon nanotube and biomass carbon activated by KOH and CO₂ gas for supercapacitor. In: *The 4th Nanoscience and Nanotechnology Symposium* 2011. p. 180–1. AIP:1415 Conf. Proc.
 - [47] Yu H, Wu J, Fan L, Xu K, Zhong X, Lin Y, et al. Improvement of the performance for quasi-solid-state supercapacitor by using PVA-KOH-KI polymer gel electrolyte. *Electrochim Acta* 2011;56(20):6881–6.
 - [48] Show Y, Imaizumi K. Electric double layer capacitor with low series resistance fabricated by carbon nanotube addition. *Diamond Relat Mater* 2007;16(4–7):1154–8.

